J. Fluid Mech. (2002), *vol.* 462, *pp.* 383–409. © 2002 Cambridge University Press
DOI: 10.1017/S0022112002008649 Printed in the United Kingdom

Instability and mode interactions in a differentially driven rotating cylinder

By J. M. LOPEZ[1], J. E. HART[2], F. MARQUES[3], S. KITTELMAN[2] AND J. SHEN[4]†

[1]Department of Mathematics and Statistics, Arizona State University, Tempe, AZ 85287-1804, USA

[2]Program in Atmospheric and Oceanic Sciences, CB311, University of Colorado, Boulder, CO 80309, USA

[3]Departament de Física Aplicada, Universitat Politècnica de Catalunya, Jordi Girona Salgado s/n, Mòdul B4 Campus Nord, 08034 Barcelona, Spain

[4]Department of Mathematics, University of Central Florida, Orlando, FL 32816-1632, USA

(Received 3 October 2001 and in revised form 21 December 2001)

The flow in a completely filled rotating cylinder driven by the counter-rotation of the top endwall is investigated both numerically and experimentally. The basic state of this system is steady and axisymmetric, but has a rich structure in the radial and axial directions. The most striking feature, when the counter-rotation is sufficiently large, is the separation of the Ekman layer on the top endwall, producing a free shear layer that separates regions of flow with opposite senses of azimuthal velocity. This shear layer is unstable to azimuthal disturbances and a supercritical symmetry-breaking Hopf bifurcation to a rotating wave state results. For height-to-radius ratio of 0.5 and Reynolds number (based on cylinder radius and base rotation) of 1000, rotating waves with azimuthal wavenumbers 4 and 5 co-exist and are stable over an extensive range of the ratio of top to base rotation. Mixed modes and period doublings are also found, and a bifurcation diagram is determined. The agreement between the Navier–Stokes computations and the experimental measurements is excellent. The simulations not only capture the qualitative features of the multiple states observed in the laboratory, but also quantitatively replicate the parameter values over which they are stable, and produce accurate precession frequencies of the various rotating waves.

1. Introduction

This paper describes a combined laboratory and theoretical/numerical study of linear and nonlinear instability and wave selection in a rotating cylinder driven by a differentially rotating lid. The laboratory experiments are used to identify regions of parameter space where multiple states, hysteresis, secondary bifurcations and chaotic dynamics arise. They also provide quantitative data that are used to validate a three-dimensional numerical model of the flow. The computational simulations are used to identify and describe the steady axisymmetric basic state, to characterize the transitions from axisymmetric to three-dimensional wavy motions, and to clarify the nature of the bifurcations that lead to periodic, quasi-periodic and chaotic states. The simulations provide detailed diagnostics and enable tracking of stable and weakly

† Present address: Department of Mathematics, Purdue University, West Lafayette, IN 47907, USA.

https://doi.org/10.1017/S0022112002008649 Published online by Cambridge University Press

unstable solution branches. Our joint laboratory/computational approach has allowed us to construct a fairly complete picture of the nonlinear dynamics of a rotating shear flow that contains a particularly rich and varied set of dynamics.

Internal shear layers appear in a number of rotating geophysical systems. Linear barotropic instabilities that convert basic flow kinetic energy into eddy kinetic energy are thought to be important for eddy and wave production in the atmosphere and oceans (e.g. Fantini & Tung 1987; Toyoda *et al.* 1999; Paldor 1999). For example, instability of the horizontally sheared zonal wind distribution in the tropics at planetary wavenumber 3 and 4 may be responsible for the 'two-day waves' in the stratosphere (Limpasuvan *et al.* 2000). Although linear theory has success in describing the initial wave growth of perturbations in a number of settings, nonlinear effects are often of great significance. Instabilities on a model intertropical convergence zone (ITCZ) undergo nonlinear wave selection and eddy clustering (Ferreira & Schubert 1997). Finite-amplitude perturbations may cause linearly stable ocean eddies to become unstable (Hua 1988). The hurricane eyewall can take on a hexagonal or polygonal shape that may be accounted for by nonlinear potential vorticity mixing following barotropic instability of a circular vortex (Schubert *et al.* 1999). Wave interpretations of Saturn's Polar Hexagon have been offered (Allison, Godfrey & Beebe 1990), but the sharp-cornered shape of the feature as observed by Voyager (Godfrey 1988) is likely to be a result of nonlinearity. For these examples the Rossby number varies from about 1/4 for Saturn's polar jets to over 1 for the tropical situations cited here. Our study of the fundamental nonlinear dynamics arising subsequent to barotropic instability in a controlled rotating system with comparable Rossby number is in part motivated by a desire to understand mechanisms that may be of potential significance in these complex geophysical problems.

The system investigated in this paper displays dynamics similar to those observed previously in related, but different, physical configurations. Rabaud & Couder (1983) and Chomaz *et al.* (1988) present experimental visualizations and results of a two-dimensional (i.e. no variation in the direction of the rotation axis) numerical calculation of the instabilities on an internal vertical shear layer driven by the differential rotation of top and bottom concentric disks mounted in the endwalls of a circular slot. The depth of the slot is small compared with its radius so that the Ekman layers fill the entire vertical gap. Because of this small aspect ratio, two-dimensional simulations are able to qualitatively capture some of the features observed experimentally, namely the steady wave hysteresis and a subharmonic state. Quantitative comparisons were poor, the order-one differences being attributed to errors in representing the basic shear flow accurately in the numerical computations.

Hide & Titman (1967) and Früh & Read (1999) performed experiments on a tall, low Rossby number system. In this case motions were driven by a vertically symmetric arrangement of differentially rotating discs embedded in the endwalls. The disc diameter was about half the cylinder diameter. In the rapidly rotating regime a vertical Stewartson layer appears, locking in place over the small gap between the embedded discs and the endwalls. This shear layer becomes unstable to a wave with azimuthal wavenumber n. Regions of stable constant-amplitude rotating waves with different but adjacent wavenumbers (e.g. n and $n+1$) overlap in parameter space, indicating the presence of multiple states. Flow visualizations suggested the existence of a phase-locked state with wavenumbers 2 and 1, and LDV output hinted at a quasi-periodic regime. Apart from qualitatively successful comparisons with quasi-geostrophic linear instability theory, there has been no attempt to simulate the supercritical states in these experiments. For the parameters of the Früh–Read

https://doi.org/10.1017/S0022112002008649 Published online by Cambridge University Press

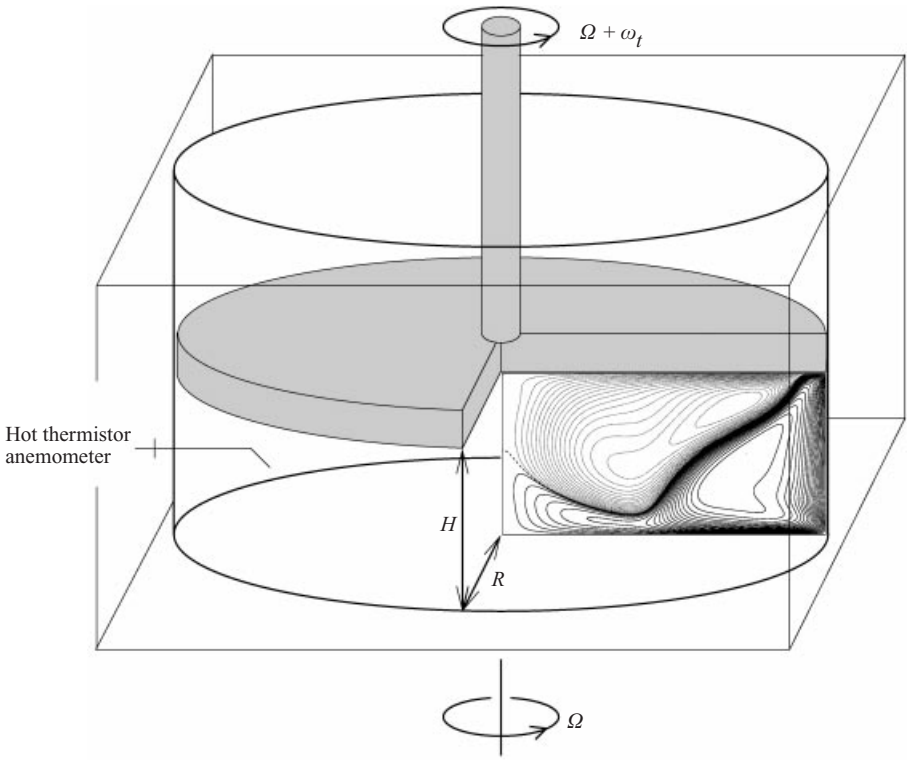


FIGURE 1. Schematic of the flow geometry. The inset illustrates typical streamlines of a steady axisymmetric flow determined by numerical simulation.

experiments this would be a daunting undertaking because of the high effective Reynolds number (as large as 10^5), and the small Ekman number (of order 10^{-4}). The latter means that Ekman layers on the horizontal surfaces occupy 1% of the height, and, especially if these boundary layers separate into the interior, the resolution requirements render accurate three-dimensional simulation impractical.

It is not surprising that these systems, together with ours, show similar qualitative dynamics. For example, the $SO(2)$ symmetry and azimuthal wavenumber quantization lead naturally to hysteresis, as has been seen in other systems with this symmetry (e.g. Hart 1980, 1981). For the reasons suggested above, however, there has not yet been a quantitatively accurate simulation of such a system that permits a detailed investigation of the nature of the bifurcations associated with primary and secondary instabilities. Thus we focus on a modest Reynolds number flow that exhibits all of the previously observed qualitative nonlinear behaviour, along with some new features.

The basic geometry is shown in figure 1. It consists of a cylinder of radius R, closed at the bottom, rotating at rate Ω, and containing a liquid of depth H and constant viscosity ν. Motions are driven by a contact top lid that differentially rotates at rate ω_t (or which rotates in the inertial frame of reference at rate $\Omega_t = \Omega + \omega_t$). There are three non-dimensional parameters for this system, two of which are held fixed here:

$$Re = \Omega R^2/\nu = 1000,$$

$$\Lambda = H/R = 0.5,$$

$$S = -\Omega_t/\Omega = -(1 + \omega_t/\Omega).$$

https://doi.org/10.1017/S0022112002008649 Published online by Cambridge University Press

In the present paper we consider the retrograde driving situation with $\omega_t < -\Omega$, so that S is positive. In this situation there is radial inflow along the upper driving surface in a nonlinear Ekman layer. For sufficiently large S, this layer separates before reaching the axis and an internal shear layer forms. The shear layer separates fluid with azimuthal velocity of the same sense as the base of the cylinder from that with the sense of the counter-rotating top. There is also a strong meridional jet-like flow along the shear layer. A detailed study of the axisymmetric basic state and its stability in an axisymmetric subspace is presented in Lopez (1998). The characteristic axisymmetric basic state is shown in figure 1. The shear layer in this example separates near the upper right corner and re-attaches at about mid-depth on the axis. In this paper, we are interested in the nonlinear dynamics associated with general three-dimensional instabilities of this shear layer.

S is between 0 and 1 in our study, so the external Rossby number $Ro = -(S+1)/2$ is between 0.5 and 1 in magnitude. The transition from axisymmetric to wavy flow is due to hydrodynamic shear flow instability. This is only weakly affected by rotation because the shear-layer local Rossby number is considerably higher than the system Rossby number. However, the basic rotation of the cylinder is crucial in setting up a detached shear layer in the interior of the fluid that is subject to such instability. System rotation is important but not so dominant as to constrain the motions to be two-dimensional in planes perpendicular to the rotation axis. Our geometry moves the discontinuity between the driving disk and the surrounding walls away from the interior (where it is located in the previous work cited above) and into the upper corner. This minimizes its affect on the interior dynamics. The system is invariant to arbitrary rotations about the axis, $SO(2)$ symmetry, and arbitrary translations in time, so the basic state is axisymmetric and steady, but with non-trivial structure in the radial and axial directions (r and z, respectively). In this paper, we study how the basic state loses stability and how subsequent finite-amplitude wavy states are selected and maintain or lose stability as S is increased. The other two governing parameters remain fixed at $Re = 1000$ and $\Lambda = 0.5$.

2. Experimental results

The laboratory cell, sketched in figure 1, has the following dimensions and characteristics:

$$R = 0.101\,\mathrm{m},$$
$$H = 0.050\,\mathrm{m},$$
$$\nu = 0.10\,\mathrm{cm^2\,s^{-1}} = 10^{-5}\,\mathrm{m^2\,s^{-1}},$$
$$\Omega = 1\,\mathrm{rad\,s^{-1}},$$
$$Re = 1000 \pm 10,$$
$$\Lambda = 0.5 \pm 0.005.$$

Figure 2 shows a photograph of the experiment. The cylinder is machined Plexiglas with a roundness of $\pm 0.03\%$. The drive lid is made of machined and black-anodized aluminium with a flatness of 0.02 mm. The gap between this 1.25 cm thick disk and the rigid Plexiglas sidewall is less than 2×10^{-4} m. The basic rotation is maintained by a d.c. servo-loop turntable with a stability of $\pm 0.02\%$. The lid is driven by a stepper motor attached to the cylinder. Its rotation rate stability is 0.2% or better. The fluids used were 10 c S silicone oil, for hot thermistor anemometry, or 10 c S glycerol, for dye injection runs. To keep viscosity constant, and to provide a known

https://doi.org/10.1017/S0022112002008649 Published online by Cambridge University Press

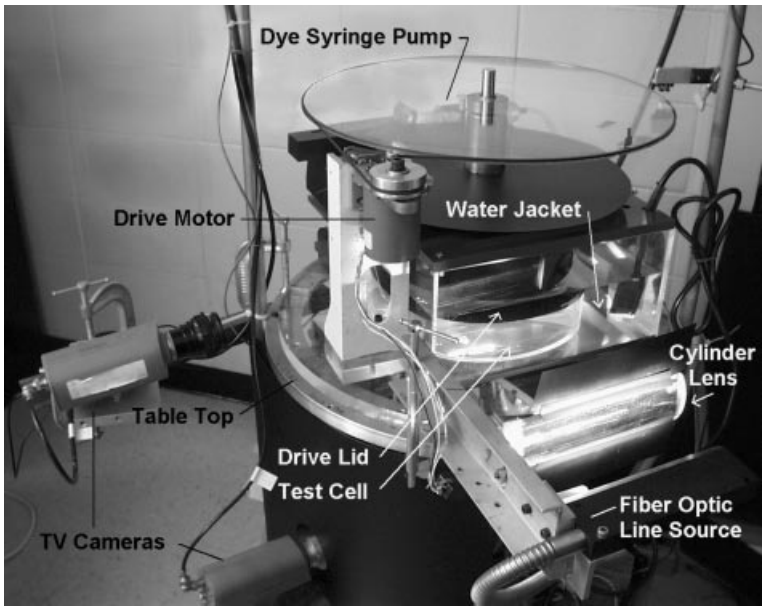


FIGURE 2. Photograph of the experiment showing the co-rotating TV cameras, fibre optic slit light, and differential drive motor. This whole apparatus sits on a rotating table.

reference temperature for our thermistor velocimeter, the experiment was immersed in a constant temperature bath. The bath was set at 24 °C and was maintained within 0.01 °C of this value over the course of the experiments.

Crude visualization was accomplished using aluminium flakes in silicone oil. Nicer photographs of the wavy states were obtained by injecting Fluorescein dye at two locations at opposite ends of a diameter just below driving disk. Since Fluorescein is not appropriate for use in silicone oil, which would have to be discarded after being saturated, these experiments used glycerol. Illumination was provided by a fibre-optic slit-light focused by a cylindrical lens. Two TV cameras, one looking up from below and one looking in from the side, imaged the dye. The temporal state of motion was determined by digitizing the output from a small hot-thermistor constant-temperature anemometer located 0.025 m in from the sidewall at a height of 0.040 m up from the transparent Plexiglas bottom. The stem of the probe is 0.0009 m in diameter, while the probe itself, sticking 0.01 m out from the stem, is 0.0005 m in diameter. A larger probe (0.0017 m) was found to disturb the flow and to change the axisymmetric-to-wavy stability boundary, when compared with non-intrusive measurements made by monitoring Kalliroscope reflectance vs. time at a fixed point using a TV camera. The smaller probe's data agreed with the optical transition measurements and has the advantage of providing relatively clean speed vs. time data from which the wave frequencies can be accurately obtained.

Figure 3 shows dye images for two extreme cases: axisymmetric steady flow and a chaotic state. For $S < 0.39$ rings of dye move in from the upper corner in the Ekman layer along the upper disk. The rings then advect down into the interior when the Ekman layer separates from the upper horizontal boundary. S is slowly increased, usually in steps of 2% with a waiting time of 300 rotations followed by a data taking interval of a similar length. For S greater than about 0.410 the dye rings break into waves. Figure 4 shows a wavenumber-4 rotating wave state, RW_4 (rotating waves are invariant spatial structures in a frame rotating at their precession frequency).

https://doi.org/10.1017/S0022112002008649 Published online by Cambridge University Press

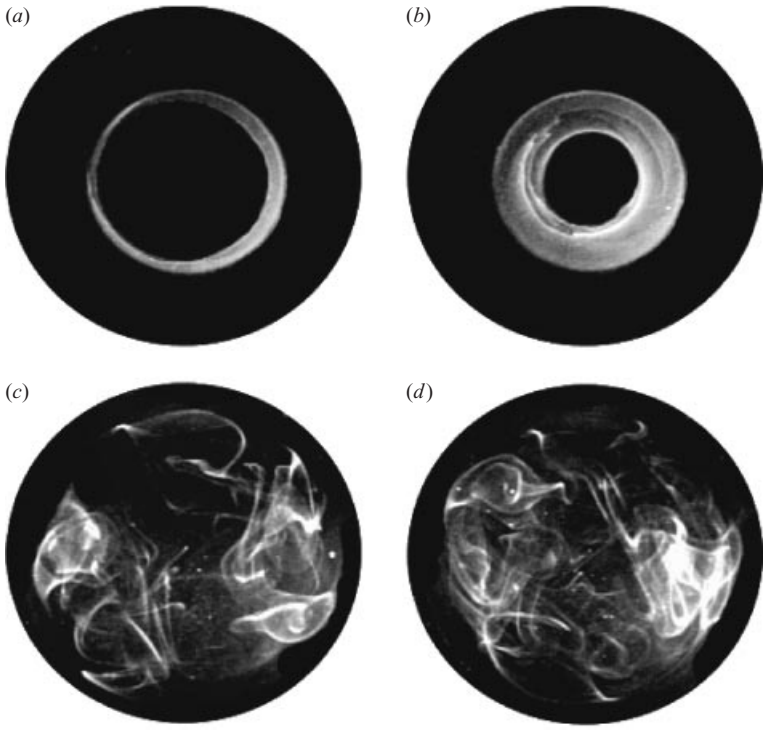


FIGURE 3. Planview of dye patterns resulting from the release of Fluorescein dye at two opposite points at the upper corner. (a, b) Axisymmetric state, $S = 0.39$ and (c, d) chaotic state, $S = 0.894$, both for $Re = 1000$ and $\Lambda = 0.5$. The temporal displacements between left and right panels are about 3 basic rotations. Photographs are taken from below, looking up at a horizontal light sheet centred on mid-depth with a thickness of about $0.5\,H$.

Even for a simple temporal state, the dye advection patterns can, over time, become quite complex, as is well known from chaotic advection studies. The sideviews of figure 4 show the separated boundary layer, diving down into the interior, with a wavenumber-4 dye structure evolving in time. The sideviews cover the approximate axial range $0.1\,H < z < 0.9\,H$. Note that the dye is released into the rotating wave state. The changes in the dye sheet structure shown in the figure are not due to spatial changes in the flow state over time, but rather reflect the advection of the (small amount of) dye (released over a 3 s interval) through the complicated spatial structure in the combined axisymmetric flow plus rotating wave state as time evolves.

For $0.41 < S < 0.72$ two distinct rotating wave states were observed. Example dye patterns of the RW_4 and RW_5 states, both at $S = 0.440$, are shown in figure 5. These photographs illustrate the regular but highly structured patterns obtained by nonlinear advection of dye in these wave fields. That these are rotating wave states is also clearly evident from frequency spectra, as illustrated in figure 6. The spectra were obtained from the thermistor speed sensor mounted on the rotating cylinder and represent frequencies in the rotating frame of reference. Although velocimeter calibration curves were obtained, for frequency analysis we just analysed the voltage output from the bridge circuit. A peak finder is used to obtain the main component frequency, which is accurate to better than 0.3%. The waves are nearly but significantly non-resonant. The phase speeds (frequency over wavenumber) are 0.949 and 0.929 for the two states in figure 6.

https://doi.org/10.1017/S0022112002008649 Published online by Cambridge University Press

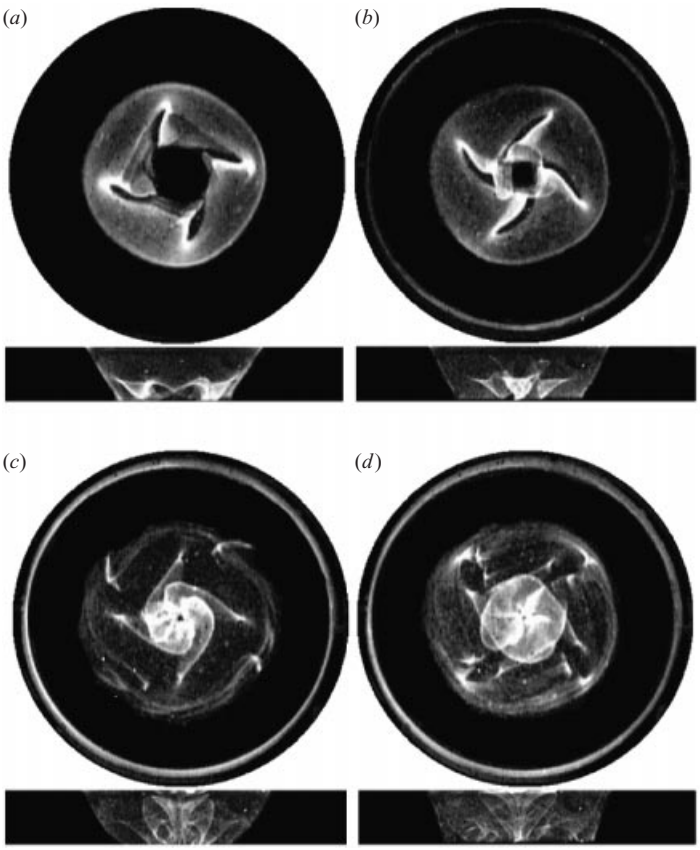


FIGURE 4. Planview and sideview of dye released into a wavenumber-4 rotating wave at $S = 0.411$. (*a–d*) Time sequence of shots at $t = 0$, 7, 19, and 24 s (basic rotation = 6.24 s). In the sideview the dye is injected at the upper corner and initially flows radially inwards in the upper Ekman layer that is not illuminated by the lateral light beam.

Figure 7 shows the variation of wave frequency with S, as would be seen in the inertial frame. The inertial-frame frequency (non-dimensionalized by the base rotation rate Ω) is the wavenumber minus the frequency of the peak obtained from the spectra (as in figure 6). Positive frequencies are plotted, but all patterns propagate retrograde (opposite to Ω) in the rotating reference frame. The RW_5 state has a higher frequency at low S and at high S. The curves cross at $S \approx 0.45$ and again at $S \approx 0.60$. At large S (greater than about 0.6), RW_5 states are harder to track or reach from random initial conditions. This suggests that the RW_5 branch becomes less stable with a smaller attractor basin as S increases. No RW_5 states were found for $S > 0.70$.

At $S = 0.78$ a period-doubling bifurcation occurs on the RW_4 branch (see figure 8). The first subharmonic of the primary wavenumber-4 frequency grows. Dye releases indicated that this is related to the appearance of a spatially phase-locked wavenumber-2 disturbance. We have not attempted to quantify the amplitude vs. supercriticality of these modes because measurements are at a fixed point and changes in the flow's spatial structure can be misinterpreted as changes in amplitude. However, there does not appear to be hysteresis in this transition.

At the same parameter point as that shown in figure 8(*b*), it is possible to find a quasi-periodic regime whose time series and spectra are shown in figure 9(*a*).

https://doi.org/10.1017/S0022112002008649 Published online by Cambridge University Press

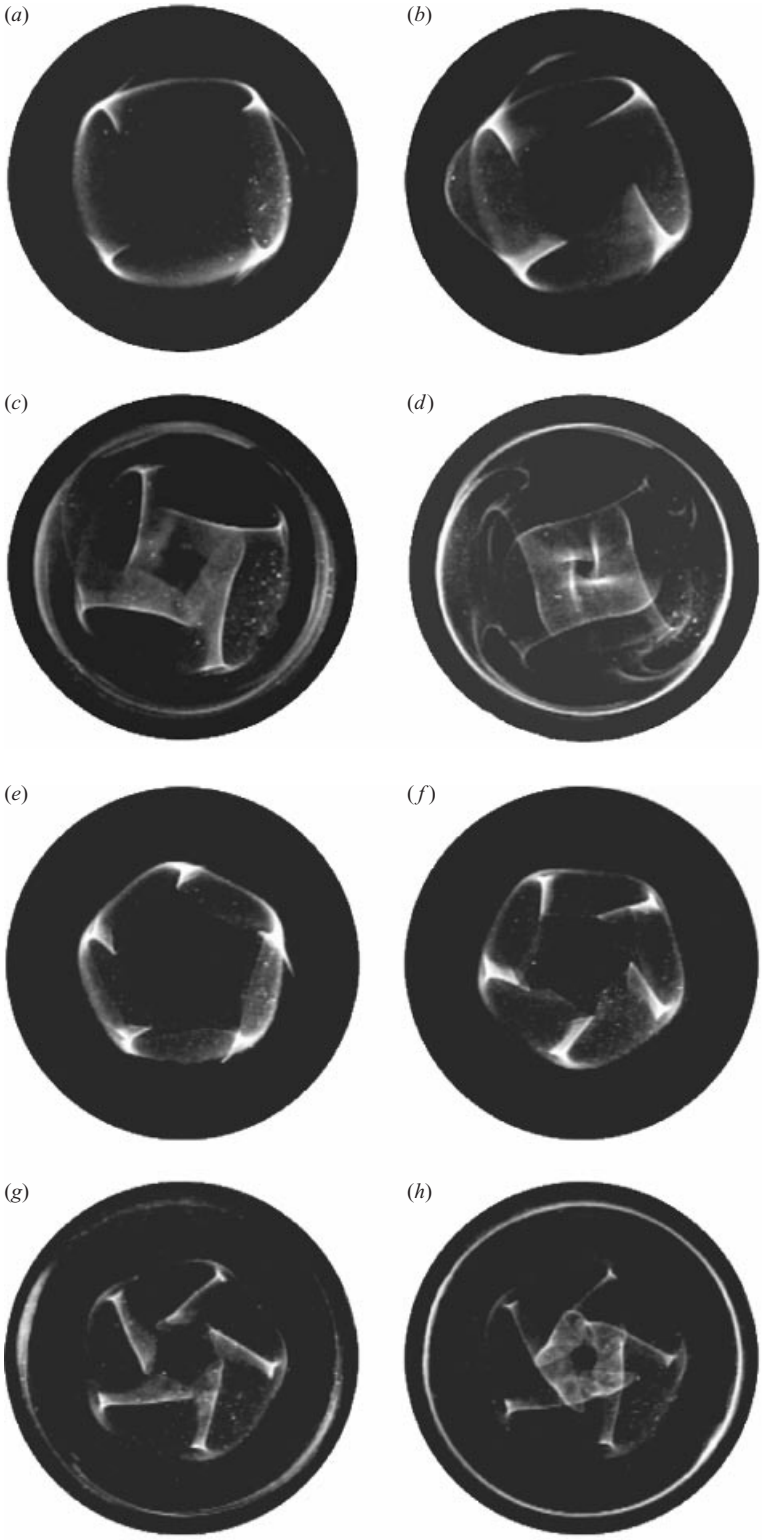


FIGURE 5. Dye sequences for $S = 0.440$: (a–d) RW_4 and (e–h) RW_5 states. The images in each sequence are approximately 10 s apart.

https://doi.org/10.1017/S0022112002008649 Published online by Cambridge University Press

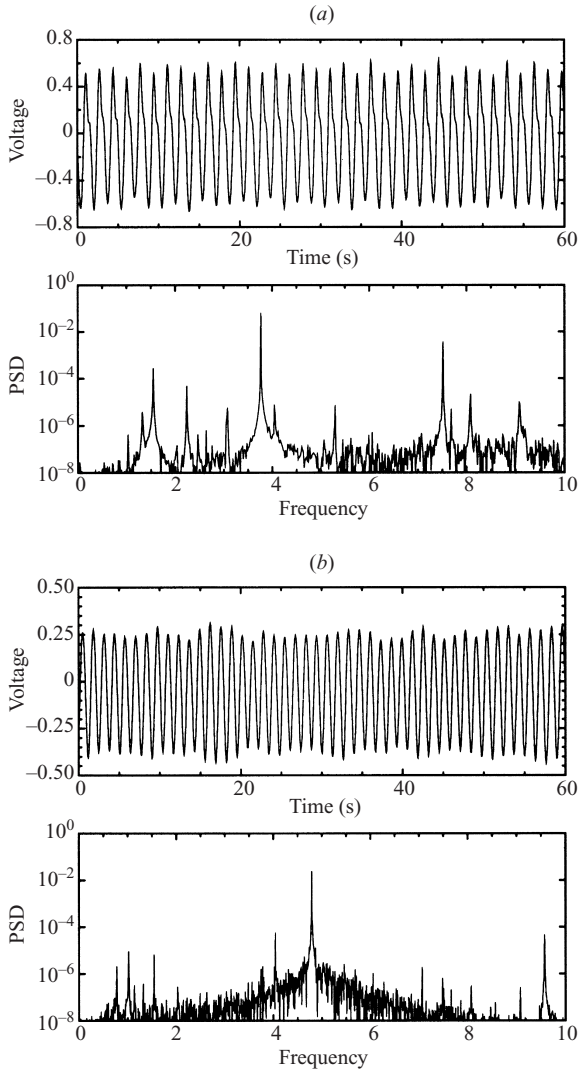


FIGURE 6. Time series and frequency spectra for (*a*) RW_4 and (*b*) RW_5, both at $S = 0.516$. Probe output was digitized at 10 Hz for a period of 2000 s. The frequency is normalized by the base rotation rate and the signal is measured in the rotating frame of reference.

The signal for this QP regime is dominated by wavenumber 4. The quasi-periodic modulation, in which the contributions of wavenumbers 4 and 2 wax and wane, arises at about one-twentieth the frequency of the dominant wave, or with frequency 0.20 (in units of Ω). The quasi-periodic state and the two-wave steady-amplitude rotating-wave state coexist over a limited range of S. Above about $S = 0.81$ only the QP form is found. Eventually, as S increases, the modulations become irregular, as illustrated in figure 9(*b*). The details of this transition, and the return to periodic and axisymmetric flow as S is raised past 1.0 will be reported in a future communication.

In summary, the experiments show rotating waves from $S = 0.41$ to $S = 0.79$. There are two states with wavenumber 4 and 5, with the latter becoming unstable (and hence not observed) past $S = 0.70$. For a range of S of about 0.02 centred on 0.79 two more-complicated states can apparently exist together. These are a spatially

https://doi.org/10.1017/S0022112002008649 Published online by Cambridge University Press

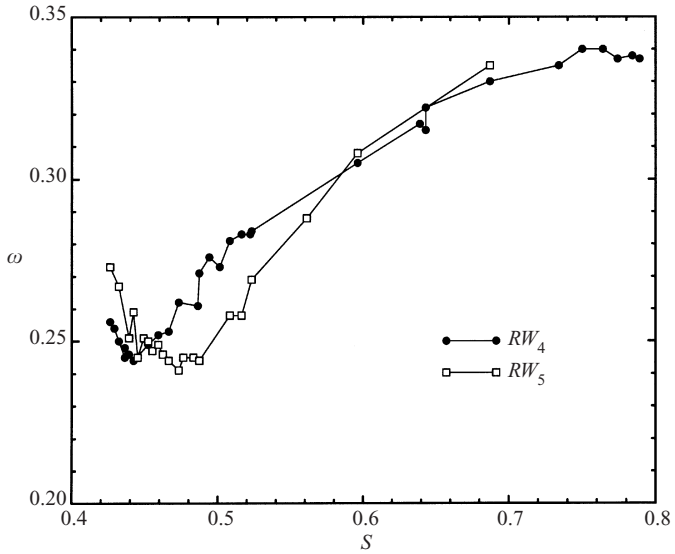


FIGURE 7. Wave frequencies as functions of S for rotating waves as would be measured in the inertial frame of reference.

and temporally period-doubled RW_4 leading to a phase-locked RW_2, and a quasi-periodic state with modulation frequency about 0.20. For S between approximately 0.81 and 0.84 only quasi-periodic states were found. For $S > 0.84$ intermittent bursts of near-periodic motions are interspersed within noisy fluctuations.

As will be shown below, these laboratory results are in remarkable agreement with numerical computations. However, one stable branch, uncovered numerically, was not found in the laboratory realizations. This is a weak quasi-periodic mixed wave state existing from $S = 0.44$ to 0.46. We tried to find this by stepping slowly forward and backwards through this region, by doing impulsive starts or jumps from stable wavenumber 5 or 4 states, or by using initial conditions from QP or chaotic states. Runs as long as 48 hours (at 6.24 s per base rotation) never relaxed to a QP state in this window. The system always equilibrated to a stable RW_4 or RW_5. One possibility is that the finite probe size may de-stabilize or otherwise damp out the weak mixed mode.

3. Governing equations and computational method

The computational simulations of the three-dimensional motions in the cell sketched in figure 1 are carried out in the inertial frame of reference. The equations governing the flow are the Navier–Stokes equations together with initial and boundary conditions. We denote the velocity vector and pressure respectively by $\boldsymbol{u} = (u, v, w)^T$ and p. Then, the non-dimensionalized Navier–Stokes equations in velocity–pressure formulation written in cylindrical coordinates are

$$\left.\begin{aligned} \partial_t u + \mathrm{adv}_r &= -\partial_r p + \frac{1}{Re}\left(\Delta u - \frac{1}{r^2}u - \frac{2}{r^2}\partial_\theta v\right), \\ \partial_t v + \mathrm{adv}_\theta &= -\partial_\theta p + \frac{1}{Re}\left(\Delta v - \frac{1}{r^2}v + \frac{2}{r^2}\partial_\theta u\right), \\ \partial_t w + \mathrm{adv}_z &= -\partial_z p + \frac{1}{Re}\Delta w, \end{aligned}\right\} \tag{3.1}$$

https://doi.org/10.1017/S0022112002008649 Published online by Cambridge University Press

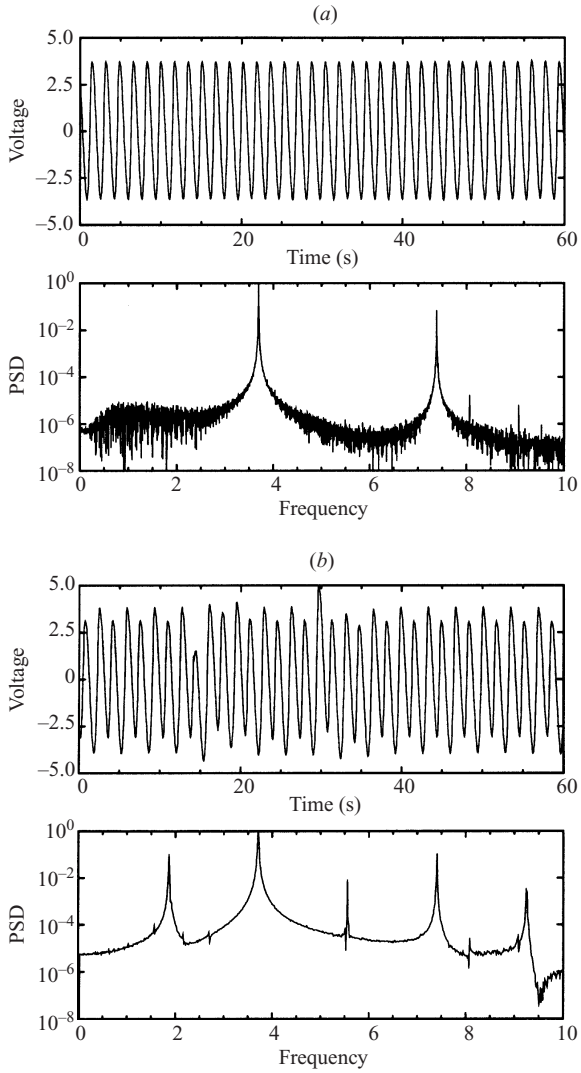


FIGURE 8. The period-doubling bifurcation from (*a*) RW_4 at $S = 0.779$ to (*b*) a phase-locked RW_2 at $S = 0.795$.

$$\frac{1}{r}\partial_r(ru) + \frac{1}{r}\partial_\theta v + \partial_z w = 0, \tag{3.2}$$

where

$$\Delta = \partial_r^2 + \frac{1}{r}\partial_r + \frac{1}{r^2}\partial_\theta^2 + \partial_z^2, \tag{3.3}$$

is the Laplace operator in cylindrical coordinates and

$$\left.\begin{aligned} \mathrm{adv}_r &= u\partial_r u + \frac{v}{r}\partial_\theta u + w\partial_z u - \frac{v^2}{r}, \\ \mathrm{adv}_\theta &= u\partial_r v + \frac{v}{r}\partial_\theta v + w\partial_z v + \frac{uv}{r}, \\ \mathrm{adv}_z &= u\partial_r w + \frac{v}{r}\partial_\theta w + w\partial_z w. \end{aligned}\right\} \tag{3.4}$$

https://doi.org/10.1017/S0022112002008649 Published online by Cambridge University Press

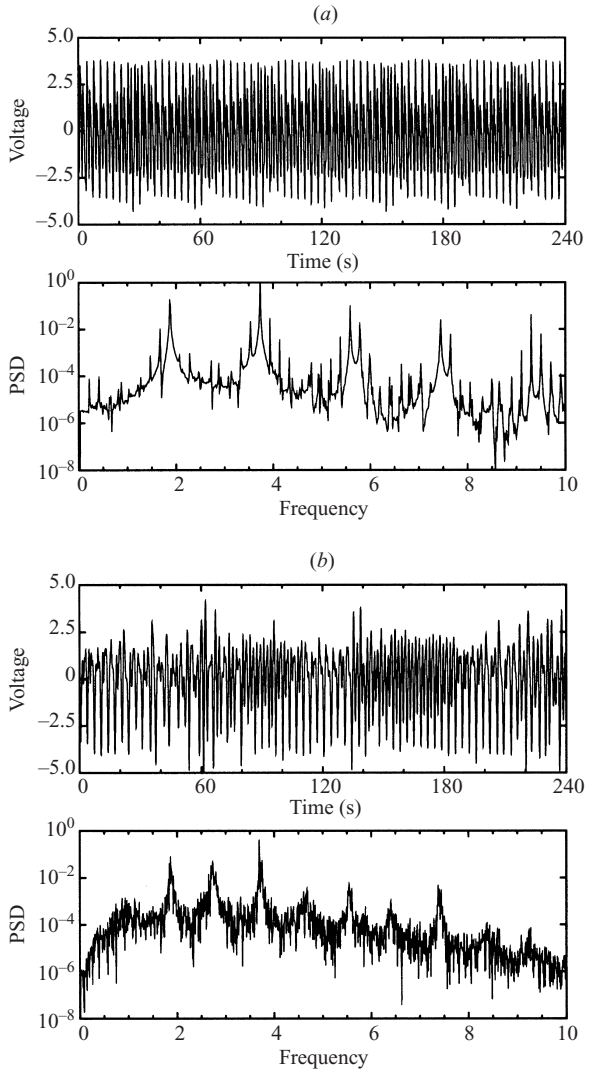


FIGURE 9. Time series and frequency spectra for (*a*) a quasi-periodic state at $S = 0.794$ and (*b*) a chaotic state at $S = 0.892$.

Note that in addition to the nonlinear coupling, the velocity components (u, v) are also coupled by the linear operators in this case. Following Orszag & Patera (1983), we introduce a new set of complex functions

$$u_+ = u + \mathrm{i}v, \quad u_- = u - \mathrm{i}v. \tag{3.5}$$

Note that

$$u = \frac{1}{2}(u_+ + u_-), \quad v = \frac{1}{2\mathrm{i}}(u_+ - u_-). \tag{3.6}$$

https://doi.org/10.1017/S0022112002008649 Published online by Cambridge University Press

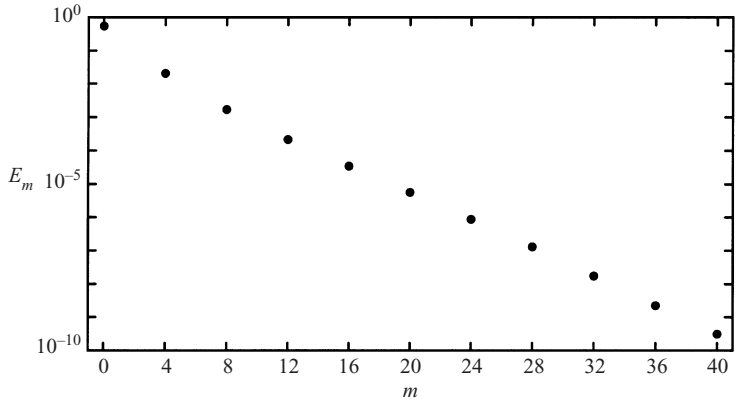


FIGURE 10. E_m for a RW_4 solution at $Re = 1000$, $S = 0.50$, $\Lambda = 0.5$, using $M = N = 32$, $L = 79$, and $\delta t = 0.005$.

The Navier–Stokes equations (3.1)–(3.2) can then be written using (u_+, u_-, w, p) as

$$\left.\begin{aligned} \partial_t u_+ + \mathrm{adv}_+ &= +\frac{1}{Re}\left(\Delta - \frac{1}{r^2} + \frac{2\mathrm{i}}{r^2}\partial_\theta\right) u_+, \\ \partial_t u_- + \mathrm{adv}_- &= -\left(\partial_r - \frac{\mathrm{i}}{r}\partial_\theta\right) p + \frac{1}{Re}\left(\Delta - \frac{1}{r^2} - \frac{2\mathrm{i}}{r^2}\partial_\theta\right) u_-, \\ \partial_t w + \mathrm{adv}_z &= -\partial_z p + \frac{1}{Re}\Delta w, \end{aligned}\right\} \tag{3.7}$$

$$\left(\partial_r + \frac{1}{r}\right)(u_+ + u_-) - \frac{\mathrm{i}}{r}\partial_\theta(u_+ - u_-) + 2\partial_z w = 0, \tag{3.8}$$

where we have denoted

$$\mathrm{adv}_\pm = \mathrm{adv}_r \pm \mathrm{i}\,\mathrm{adv}_\theta. \tag{3.9}$$

The boundary conditions are no slip on the cylinder sidewall, top and bottom:

sidewall $(r = 1)$: $u = w = 0,\ v = 1$;
bottom $(z = 0)$: $u = w = 0,\ v = r$;
top $(z = \Lambda)$: $u = w = 0,\ v = Sr$.

On the axis, the minimal (essential) pole conditions are imposed to ensure regularity of the velocity field at $r = 0$ (see Lopez, Marques & Shen 2002, for details).

The main difficulty in numerically solving the above equations is due to the fact that the velocity vector and the pressure are coupled together through the continuity equation. An efficient way to overcome this difficulty is to use a so-called projection scheme. Here, we use a stiffly stable semi-implicit, i.e. the linear terms are treated implicitly while the nonlinear terms are explicit, second-order projection scheme. For the space variables, we use a Legendre–Fourier approximation. The azimuthal direction is discretized using a Fourier expansion with $k + 1$ modes corresponding to azimuthal wavenumbers $m = 0, 1, 2, \ldots k/2$. The axial and radial directions are discretized with a Legendre expansion, as was done for the axisymmetric version of this problem (Lopez 1998). With the above discretization, one only needs to solve, at each time step, a Poisson-like equation for each of the velocity components and for pressure. These Poisson-like equations are solved using a spectral–Galerkin method, see Lopez & Shen (1998) and Lopez *et al.* (2002) for details and convergence tests. The modal energies, E_m, for a typical rotating wave solution with azimuthal wavenumber 4,

https://doi.org/10.1017/S0022112002008649 Published online by Cambridge University Press

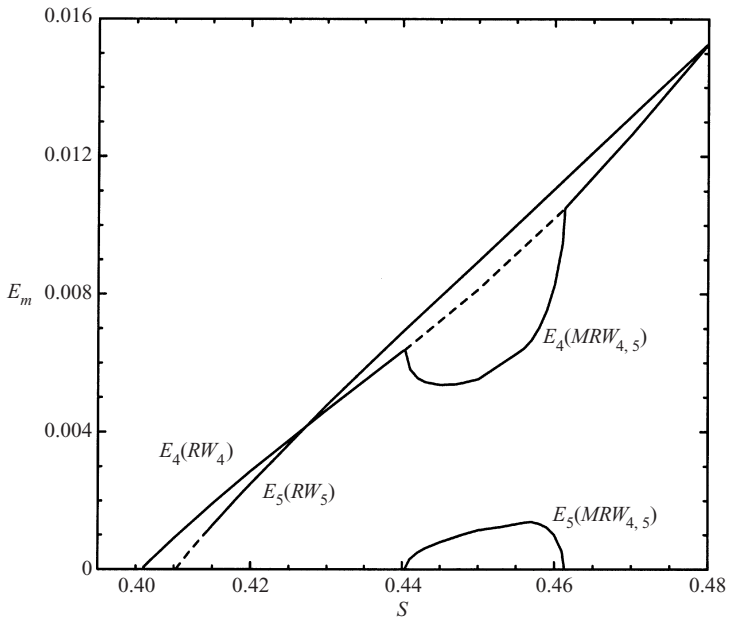


FIGURE 11. Variation with S of the zonal energies, E_m, for $Re = 1000$, $\Lambda = 0.5$; the states P_1 (RW_4), P_2 (RW_5), and P_4 ($MRW_{4,5}$) are as in figure 12. Solid lines correspond to stable states and dashed lines to unstable states.

i.e. RW_4, are plotted in figure 10, where

$$E_m = \int_0^{\Lambda} \int_0^1 \langle e_m \rangle r \, \mathrm{d}r \, \mathrm{d}z,$$

and

$$\langle e_m \rangle = \frac{1}{2} \int_0^{2\pi} \boldsymbol{u}_m \cdot \bar{\boldsymbol{u}}_m \, \mathrm{d}\theta$$

is the azimuthally averaged modal energy density. This solution, corresponding to $Re = 1000$, $S = 0.50$, and $\Lambda = 0.5$, was computed with 32 Legendre modes, M and N, in r and z, and 80 Fourier modes, $k = 79$, in θ, and time step $\delta t = 0.005$; all the results presented here have this spatial and temporal resolution.

4. Numerical results

From Lopez (1998), we have that the basic state at $Re = 1000$, $\Lambda = 0.5$ is stable to axisymmetric ($m = 0$) perturbations over an extensive range of S. When non-axisymmetric perturbations to the basic state are considered, it loses stability as S is increased beyond 0.408 to a rotating wave state with azimuthal wavenumber $m = 4$, denoted as RW_4. This is a supercritical symmetry-breaking Hopf bifurcation; figure 11 shows that $E_4(RW_4)$ grows linearly with $|S - S_{cr4}|$, where S_{cr4} is the value of S at the Hopf bifurcation. This branch of solutions can be followed by continuation (i.e. taking an RW_4 solution at a value of S as initial condition for a slightly larger value of S) up to $S = 0.441$. However, if we take different initial conditions around $S = 0.42$, some of these evolve to a rotating wave solution with azimuthal wavenumber $m = 5$, RW_5. This branch can be continued down to $S = 0.4146$, and extended out to $S = 0.699$. Note that RW_5 does not bifurcate directly as a stable solution from the basic state.

https://doi.org/10.1017/S0022112002008649 Published online by Cambridge University Press

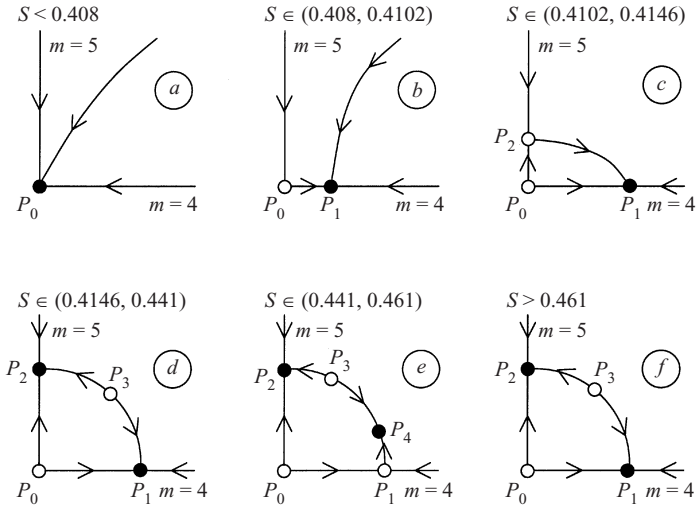


FIGURE 12. Bifurcation diagram for $Re = 1000$, $\Lambda = 0.5$ as S is varied; ● and ○ correspond to stable and unstable solutions respectively, the state P_0 is the steady axisymmetric basic state, P_1 and P_2 are RW_4 and RW_5 rotating waves, respectively, and P_3 and P_4 are modulated rotating waves with mixed azimuthal wavenumbers $m = 4$ and 5 (the stable one of the two, we denote $MRW_{4,5}$).

Continuing the RW_5 branch to smaller S by small increments, we can for short times stay arbitrarily close to the unstable RW_5 branch, all the way to the basic state at $S = 0.4102$ (which itself is unstable, having undergone the aforementioned Hopf bifurcation at $S = 0.408$ to RW_4). This is also illustrated in figure 11, where it is shown that $E_5(RW_5)$ varies linearly with $|S - S_{cr5}|$. We infer that the unstable RW_5 branch bifurcates from the unstable basic state via a supercritical Hopf bifurcation, and then subsequently at $S = 0.4146$ becomes stable. The simplest scenario consistent with this is a supercritical Neimark–Sacker bifurcation resulting in an unstable 2-torus being spawned, never observed directly, as the RW_5 branch becomes stable.

At $S = 0.441$, the RW_4 branch undergoes a supercritical Neimark–Sacker bifurcation, leading to a stable 2-torus. This new solution is a mixed mode, a modulated rotating wave with wavenumbers $m = 4$ and 5, denoted as $MRW_{4,5}$. In figure 11, $E_5(MRW_{4,5})$ is shown to grow linearly from zero and $E_4(MRW_{4,5})$ decreases from the value of $E_4(RW_4)$ at the bifurcation. As S is further increased, $MRW_{4,5}$ undergoes a reverse Neimark–Sacker where the mixed mode is absorbed back into the RW_4 branch, which is re-stabilized in the process. RW_4 continues to be stable up to $S = 0.7738$. This sequence of bifurcations resulting in the stable mixed mode is robust to spatial and temporal resolution, with no changes when the time step, δt, is doubled and the number of Fourier modes, L, is halved. This mixed mode branch is the one mentioned in § 2 that could not be detected experimentally.

The sequences of bifurcations described above are schematically summarized in figure 12. The first four panels in the figure, (*a–d*), are typical of double Hopf bifurcation scenarios. However, the Neimark–Sacker bifurcations depicted in panels (*e*) and (*f*) involving $MRW_{4,5}$ are not part of such scenarios (e.g. see Guckenheimer & Holmes 1986; Kuznetsov 1998). Note that RW_4 and RW_5 bifurcate from the basic state at very similar values of S, and one may expect that at nearby values of Re and Λ they bifurcate simultaneously. Double Hopf dynamics seems to be fairly common in rotating flows with shear (e.g. see Moroz & Holmes 1984; Churilov & Shukhman 1992; Marques, Lopez & Shen 2002).

https://doi.org/10.1017/S0022112002008649 Published online by Cambridge University Press

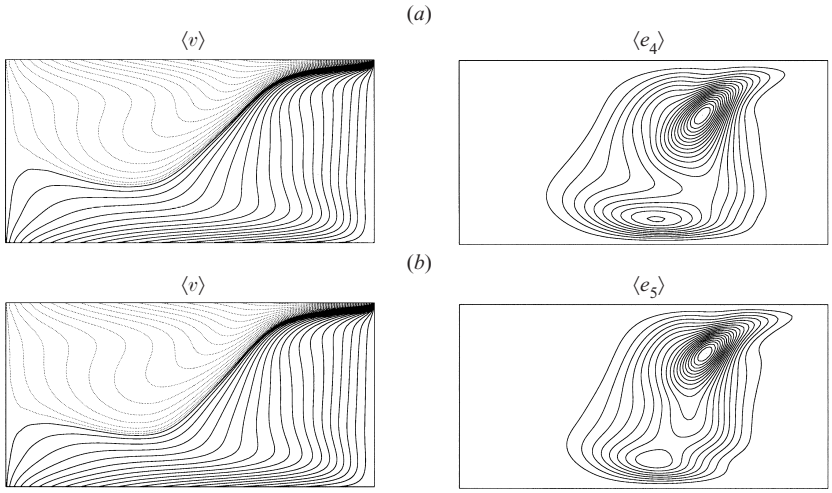


FIGURE 13. Contours of the azimuthally averaged azimuthal velocity $\langle v \rangle$, and azimuthally averaged modal energy density $\langle e_m \rangle$, for (*a*) RW_4 and (*b*) RW_5, at $S = 0.500$; $\max(e_4) = 2.5 \times 10^{-3}$ and $\max(e_5) = 2.1 \times 10^{-3}$.

Figure 13 shows contours of the azimuthally averaged azimuthal velocity, $\langle v \rangle$, and azimuthally averaged modal energy densities, $\langle e_4 \rangle$ and $\langle e_5 \rangle$, for the two rotating wave states RW_4 and RW_5 at $S = 0.500$. Both rotating waves have similar azimuthally averaged flows, and do not differ appreciably from the axisymmetric basic state at the same values of Re, Λ and S (given in figure 6(*a*) of Lopez 1998). The energy in the axisymmetric component of these states, $E_0 \sim 0.5$, is two orders of magnitude larger than the energy in the respective dominant azimuthal modes, E_4 and E_5. In both rotating waves, the energy in their non-axisymmetric components is concentrated at the shear layer formed by the separation of the Ekman layer at the top counter-rotating lid. A distinguishing feature is how these components interact with the Ekman layer on the bottom endwall; $\langle e_4 \rangle$ has a comparatively more intense local maximum near the lower endwall. The reason for this becomes clear on examining the three-dimensional structure of these solutions.

Figure 14 shows contours of the azimuthal and axial components of velocity, v and w, in a horizontal plane at $z = 0.5\Lambda$ looking down from above (the rotation of the bottom and sidewall is counter-clockwise and the top lid is rotating in the clockwise direction in this view) for RW_4 and RW_5, both at $S = 0.500$. The azimuthal instability manifests itself near the top, where the corresponding energy is largest, as a circular 'cat's-eye' pattern, typical of shear layer instabilities. The associated vortex-like structures, funnels, tend to initially extend vertically downwards and then are turned into the bottom Ekman layer, whereas in contrast, the mean shear layer becomes horizontal and attaches to the axis at about mid-height. A three-dimensional view of these (as isosurfaces of the vertical velocity) is provided in figure 15 for both RW_4 and RW_5. Figure 16 shows contours of the axial component of vorticity, ζ, at heights $z = 0.25\Lambda$ and 0.5Λ for the RW_4 and RW_5 cases in figure 14. At $z = 0.5\Lambda$, the fluid above the shear layer is rotating with negative ζ, whereas at the lower level, the funnels have decended and are locally counter-rotating with negative ζ surrounded by fluid with large positive ζ. The funnels have relatively large velocity in their cores (as indicated in figure 15), which advects the locally counter-rotating fluid down into the Ekman layer. This mechanism is a three-dimensional process;

https://doi.org/10.1017/S0022112002008649 Published online by Cambridge University Press

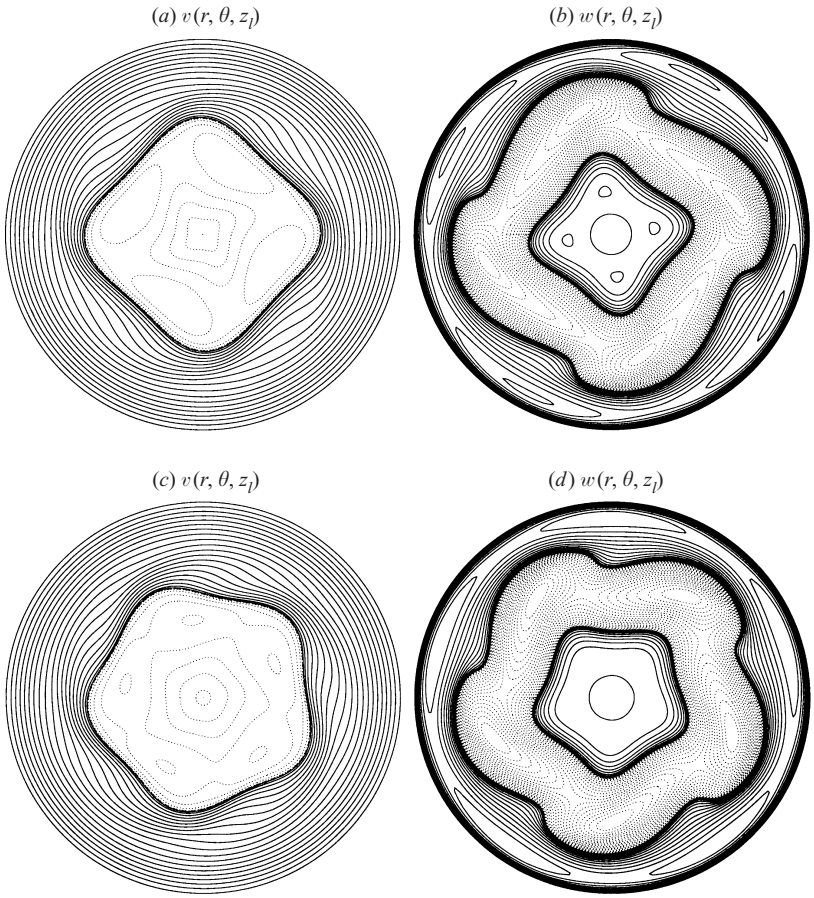


FIGURE 14. Contours of v and w on a plane at height $z_l = 0.5\Lambda$ for (a, b) RW_4 and (c, d) RW_5, both with $S = 0.500$. Contour ranges are min–max$(v, w) = (\pm 1.0, \pm 0.1)$, positive (negative) contours are solid (dashed).

there is no corresponding mechanism in the quasi-two-dimensional, low-aspect-ratio rotating shear layers, for example, studied experimentally and numerically by Rabaud & Couder (1983), Chomaz *et al.* (1988) and Bergeron *et al.* (2000).

The frequencies, ω, of the rotating wave solutions have been determined from the spectra of the time series of $V = v(0.5, 0.0, \Lambda/2)$, PSD$(V)$, and the sense of rotation (in the stationary frame) from movie animations of the solutions. For both RW_4 and RW_5, the wave structure rotates in the same direction as the bottom and the sidewall, but with smaller frequency (in the rotating frame of reference, the pattern drifts retrograde). For a rotating wave with azimuthal wavenumber m, the precession frequency is given by ω/m and the corresponding precession period is $2\pi m/\omega$. The frequencies for RW_4 and RW_5 are plotted in figure 17. The corresponding precession frequencies are approximately a factor of 20 smaller than that of the bottom and sidewall whose frequency is 1, and that of the counter-rotating top is S. These are in excellent overall agreement with the experimentally determined precession frequencies (figure 7), particularly for $S > 0.5$. For $S < 0.5$, the experimental frequencies are about 10% higher than the computed values. A possible reason for this may be related to the mixed-mode $MRW_{4,5}$ that was computed but not unambiquously identified in the experiments.

https://doi.org/10.1017/S0022112002008649 Published online by Cambridge University Press

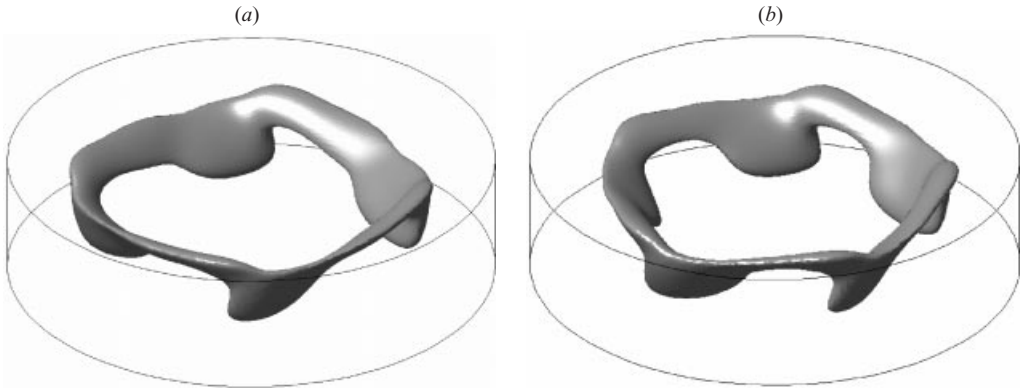


FIGURE 15. Isosurfaces of the vertical velocity, at two-thirds of the maximum downwards value, for (*a*) RW_4 and (*b*) RW_5, at $S = 0.500$; viewed slightly from above.

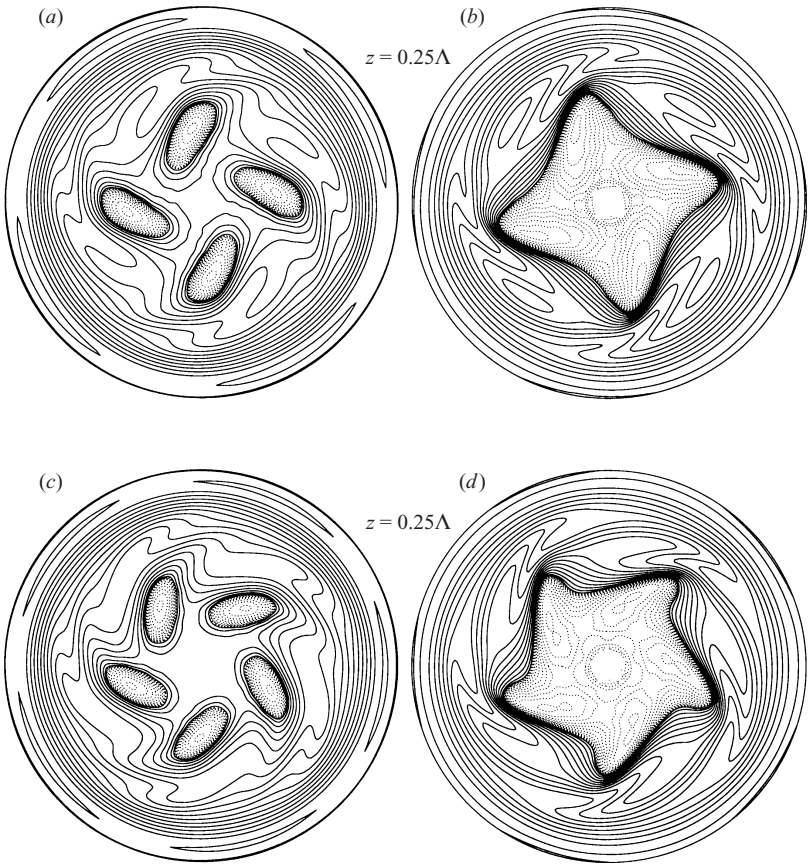


FIGURE 16. Contours of ζ on planes at height $z = 0.25\,\Lambda$ and $z = 0.5\,\Lambda$ for (a,b) RW_4 and (c,d) RW_5, with $S = 0.500$. Contour ranges are min–max$(\zeta) = (-2, 12)$, positive (negative) contours are solid (dashed).

The azimuthal average of the mixed mode $MRW_{4,5}$ is essentially the same as that of RW_4 and RW_5 (compare figures 13 and 18). Further, the structure of its $\langle e_4 \rangle$ and $\langle e_5 \rangle$ are very similar to the corresponding $\langle e_4 \rangle$ of RW_4 and $\langle e_5 \rangle$ of RW_5, although the maximum value of $\langle e_5 \rangle$ is considerably smaller, as the mixed mode bifurcates

https://doi.org/10.1017/S0022112002008649 Published online by Cambridge University Press

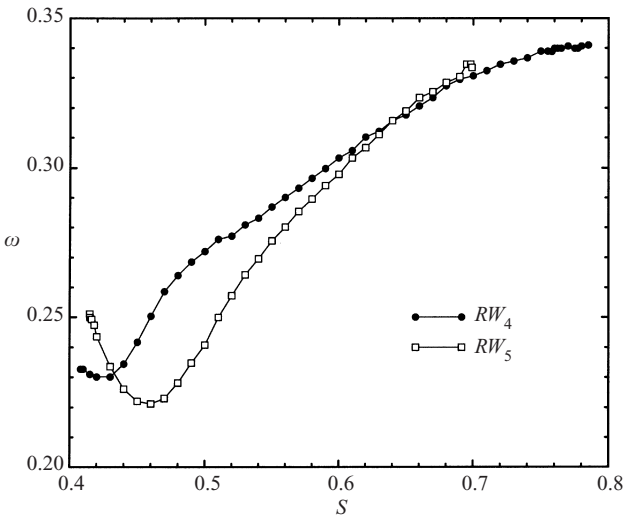


FIGURE 17. Variation of the frequencies of RW_4 and RW_5 with S, for $Re = 1000$ and $\Lambda = 0.5$.

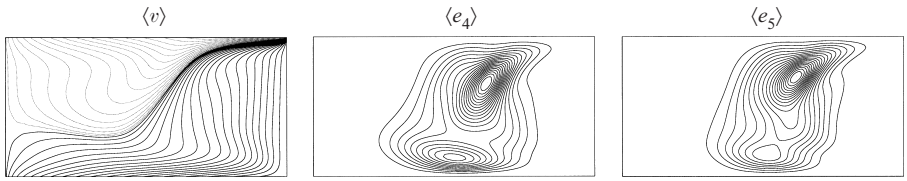


FIGURE 18. Contours of the azimuthally averaged azimuthal velocity and azimuthally averaged modal energy density for $MRW_{4,5}$ at $S = 0.450$; $\max(e_4) = 6.9 \times 10^{-4}$, $\max(e_5) = 1.3 \times 10^{-4}$.

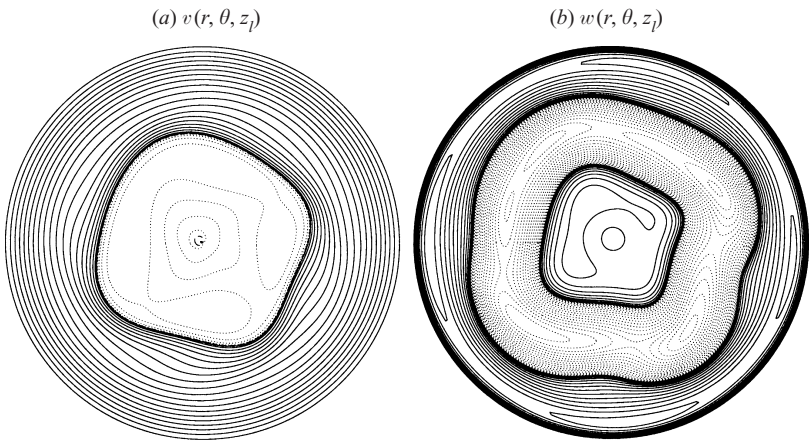


FIGURE 19. Contours of v and w on a plane at height $z_l = 0.5\,\Lambda$ for $MRW_{4,5}$ with $S = 0.450$. Contour ranges are $\min$–$\max(v, w) = (\pm 1.0, \pm 0.1)$, positive (negative) contours are solid (dashed).

from RW_4 with an $m = 5$ component being excited. The three-dimensional structure of $MRW_{4,5}$ is a small perturbation on RW_4 by the $m = 5$ component, as can been seen by comparing figures 14(a, b) and 19. The precession of the structure is roughly the same as that of RW_4 at the same values of S, but it is weakly modulated. The power spectral density of the time series of V for $MRW_{4,5}$ at $S = 0.450$ is given in

https://doi.org/10.1017/S0022112002008649 Published online by Cambridge University Press

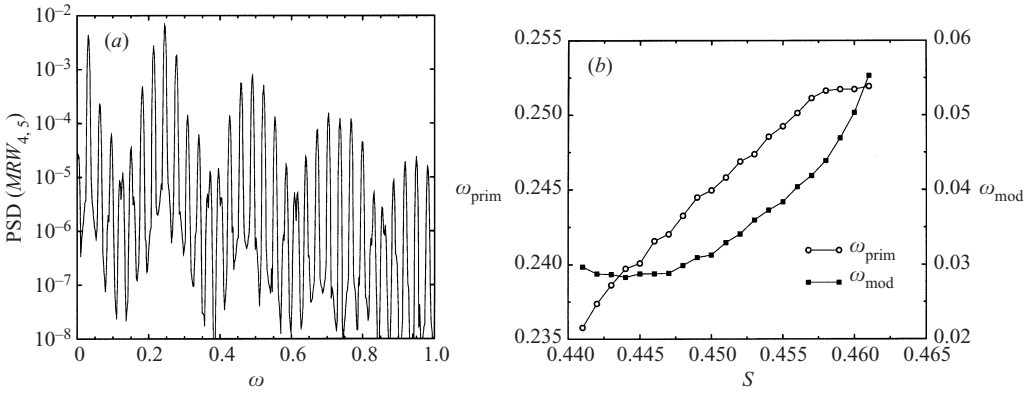


FIGURE 20. (*a*) Power spectral density of the time series of V for $MRW_{4,5}$ at $S = 0.450$, and (*b*) the corresponding primary ω_{prim} and modulation ω_{mod} peaks over the range of S in which the mixed mode exists.

figure 20. The spectrum contains a primary peak $\omega_{prim} \approx 0.245$, and another much smaller (modulation) peak $\omega_{mod} \approx 0.031$. Note that $\omega_{prim} - \omega_{mod} \approx 0.214$ and that 0.245 and 0.214 are very close to the frequencies of RW_4 and RW_5 at $S = 0.450$ (from figure 17), respectively 0.242 and 0.222. From animations the $MRW_{4,5}$ solutions appear very similar to the RW_4 state, perturbed at the shear layer (see figure 18), overall the structures (which are no longer rigid) rotating in the same sense and with very similar frequency to the corresponding RW_4, and there is also an $m = 1$ mode evident most clearly near the axis (arising from convolution between the $m = 4$ and $m = 5$ components) that rotates in the opposite sense with frequency ω_{mod}.

The rotating wave RW_4 loses stability at $S = 0.7738$ via a period-doubling bifurcation (Floquet multiplier crossing the unit circle through -1) and the RW_2 solution branch results. The modal energy $E_2(RW_2)$ grows linearly from zero with S and $E_4(RW_2)$ decreases from the value of $E_4(RW_4)$ at the critical S value (see figure 21). The power spectral density of RW_4 at $S = 0.770$ (before the period-doubling bifurcation) and of the bifurcated RW_2 at $S = 0.775$ are shown in figure 22, clearly demonstrating the doubling of the temporal period.

Comparing the structure of RW_2 at $S = 0.775$ with that of RW_4 at the same S (for which it is unstable, but by continuity we can remain arbitrarily close to the unstable RW_4 for a short time), the period doubling is most evident near the axis. From figure 23, we find that the energy in the $m = 2$ mode, $\langle e_2 \rangle$, is concentrated in the lower Ekman layer near the axis. Comparing $\langle v \rangle$, $(\langle u \rangle, \langle w \rangle)$, and $\langle e_4 \rangle$ from RW_2 with those from RW_4 (figure 13*a*), the basic characteristics of the averaged RW_2 are similar to those of RW_4. One distinguishing effect of the period doubling is how the shear layer meets the axis: for RW_4, the attachment occurred at about mid-height, whereas with $\langle e_2 \rangle$ being maximum on the axis near the bottom, the shear layer of RW_2 attaches to the axis much closer to the top.

The locally counter-rotating funnel structures on the shear layer are more prevalent at larger S, as is evident from the contours of w in figures 24(*a*) and 24(*b*). Figure 25 presents contours of v in meridional planes at $\theta = 30^\circ$ and 140°; the zero-contour level demarkates the shear layer. The horn-shaped structure of the funnel at $\theta = 30^\circ$ is very evident as it is sucked into the Ekman layer.

Continuation of RW_2 beyond $S = 0.790$ is not possible; the system evolves to a state which has the same azimuthal modal structure, but with E_0 being time-periodic

https://doi.org/10.1017/S0022112002008649 Published online by Cambridge University Press

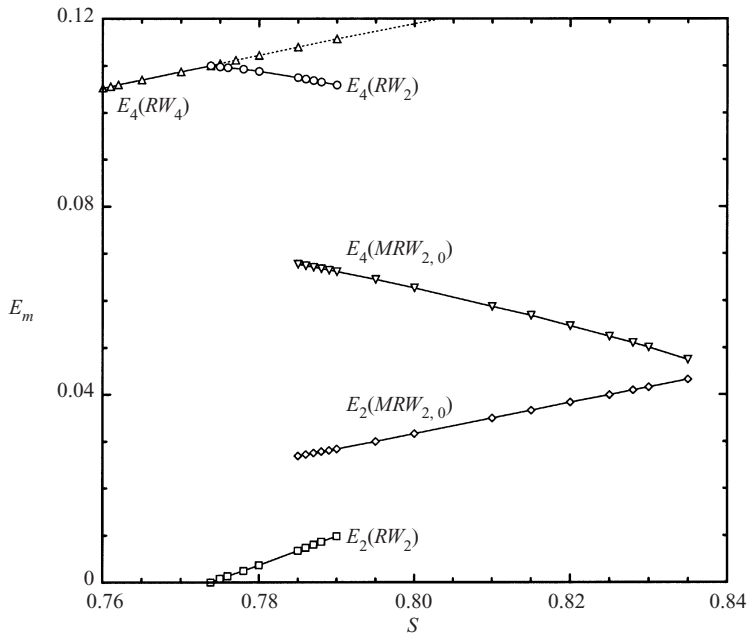


FIGURE 21. Modal energies, E_2 and E_4, of RW_2, RW_4 (dotted line denotes the unstable part of the branch), and $MRW_{2,0}$ in the neighbourhood of S where the period-doubling bifurcation from RW_4 to RW_2 and the double fold bifurcation linking RW_2 and $MRW_{2,0}$ take place.

(NB for a pure rotating wave, the modal energies are constant since the spatial structure is frozen in a frame rotating at the precession frequency). Continuing this new branch down to lower S, at $S \approx 0.785$ we return to the RW_2 branch, completing a hysteresis loop. Figure 26(a) shows E_0 for both RW_2 (for which this modal energy is steady) and the new branch that we denote $MRW_{2,0}$ (periodic) at the same $S = 0.786$. This new branch corresponds to the quasi-periodic states observed experimentally for this range of S. Figures 26(b) and 26(c) are the power spectra of V of the two states at $S = 0.786$, showing typical spectra of a pure rotating wave, (b), and (c) the same spectra with a modulation (compare with the experimentally determined spectra of the corresponding states in figures 8b and 9a).

The existence of the hysteresis loop suggests cyclic-fold bifurcations (i.e. saddle-node bifurcations of limit cycles) at each end, and the presence of an unstable branch completing the connection. This is illustrated schematically in figure 27. The presence of such folds and saddle-node bifurcations in this flow has previously been described for the axisymmetric case (Lopez 1998), but there the fold-cusp occurs at large Re. The fold bifurcations come about due to a competition between the shear layer attaching to the axis near the top or the bottom Ekman layers, as in the axisymmetric case. The shear layer originates in the top corner where the sidewall meets the counter-rotating top; where it terminates depends on the relative angular momentum of the fluid either side of it. For smaller S, the fluid above the shear layer has less angular momentum than the fluid below it, and by centrifugal effects moves towards the axis relative to the lower high-angular momentum fluid. As it does so, the shear layer tends to attach at the axis near the bottom as the central region tends to fill with the lower-angular-momentum fluid above the shear layer. For larger S, the fluid above the shear layer has more angular momentum and this fluid tends to be centrifuged radially outwards,

https://doi.org/10.1017/S0022112002008649 Published online by Cambridge University Press

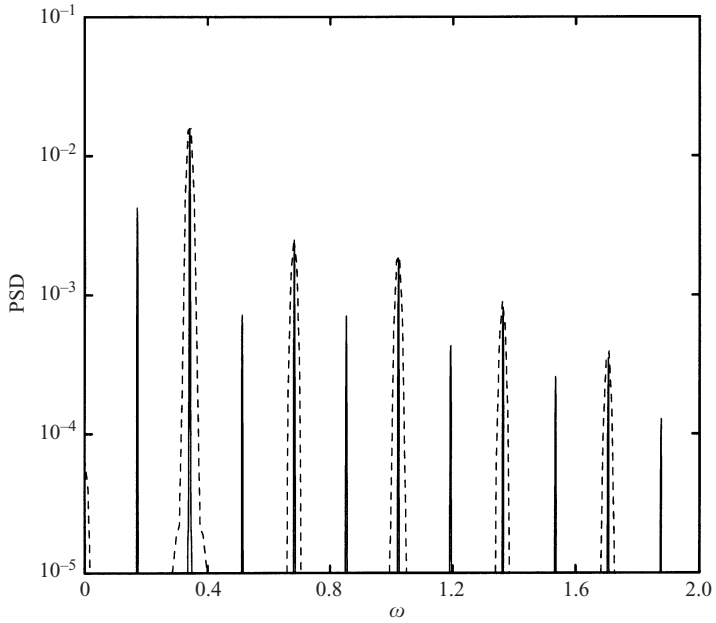


FIGURE 22. Power spectral densities of RW_4 (dashed lines) at $S = 0.770$ and RW_2 (solid lines) at $S = 0.775$.

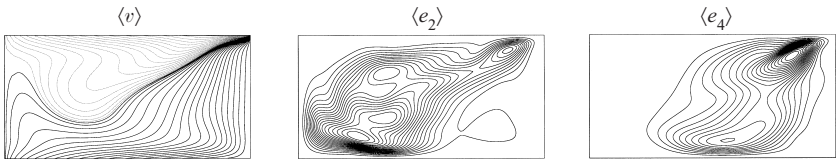


FIGURE 23. Contours of the azimuthally averaged azimuthal velocity and azimuthally averaged modal energy density for RW_2 at $S = 0.775$; $\max(e_2) = 6.3 \times 10^{-5}$, $\max(e_4) = 1.3 \times 10^{-2}$.

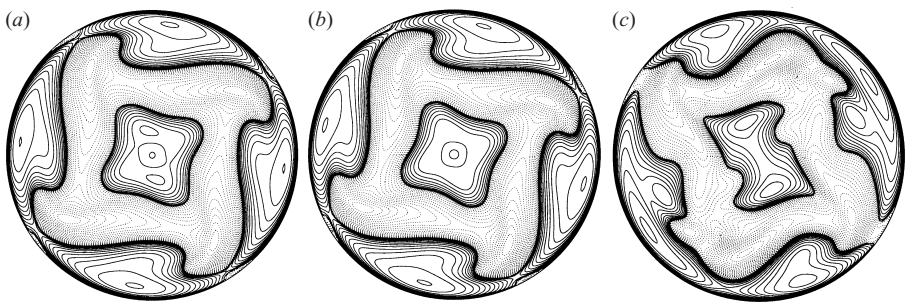


FIGURE 24. Contours of w on a plane at height $z_l = 0.5\Lambda$ for (*a*) RW_2 with $S = 0.775$, (*b*) (unstable) RW_4 with $S = 0.775$, and (*c*) $MRW_{2,0}$ with $S = 0.800$ at one instant. Contour ranges are min–max$(w) = \pm 0.2$, positive (negative) contours are solid (dashed).

the fluid below the shear layer near the axis (which has relatively small angular momentum) is drawn in to fill the void left by the centrifuged fluid, and in effect the shear layer attaches to the axis much closer to the top. The hysteresis occurs at intermediate S values. Now, in our non-axisymmetric problem, the fold bifurcations are more complex since RW_2 is a limit cycle and $MRW_{2,0}$ is a 2-torus, and so a

https://doi.org/10.1017/S0022112002008649 Published online by Cambridge University Press

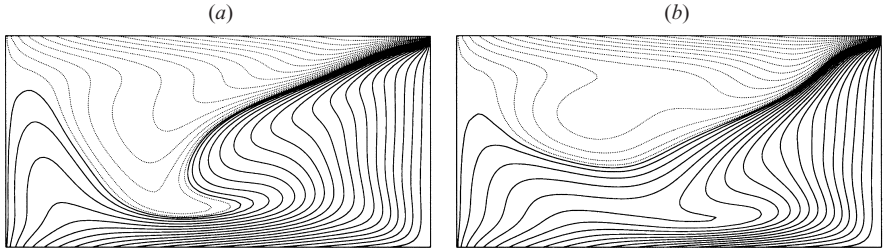


FIGURE 25. Contours of v in meridional planes at (a) $\theta = 30°$ and (b) $\theta = 140°$ for RW_2 at $S = 0.775$.

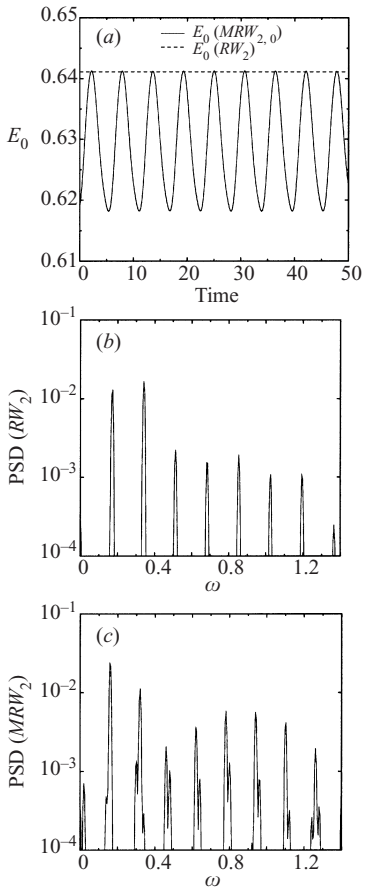


FIGURE 26. (a) Segments of the time series of E_0 for RW_2 and $MRW_{2,0}$ at $S = 0.786$, (b) and (c) power spectral densities of V from RW_2 and $MRW_{2,0}$, respectively, at $S = 0.786$.

further bifurcation must occur, introducing the second frequency in $MRW_{2,0}$, along the unstable branch. We infer that this is a Neimark–Sacker bifurcation, indicated schematically in the figure. Note that the point SN_1 is a saddle-node of limit cycles (rotating waves) and SN_2 is a saddle-node of 2-tori (modulated rotating waves).

We can further distinguish between RW_2 and $MRW_{2,0}$ by examining their azimuthal averages. For RW_2, these have already been presented in figure 23, and for $MRW_{2,0}$

https://doi.org/10.1017/S0022112002008649 Published online by Cambridge University Press

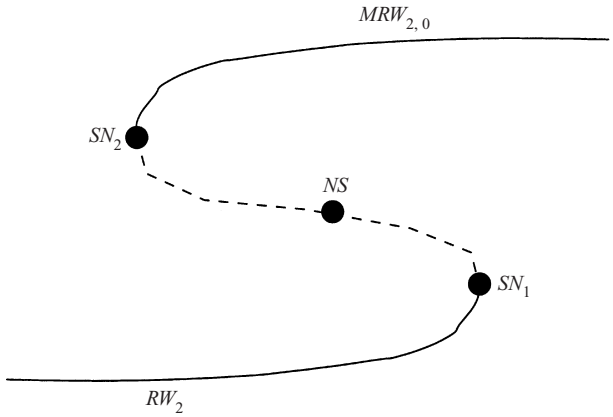


FIGURE 27. Schematic of the two-fold and intermediate Neimark–Sacker bifurcations along the RW_2 branch, resulting in the $MRW_{2,0}$ solution branch.

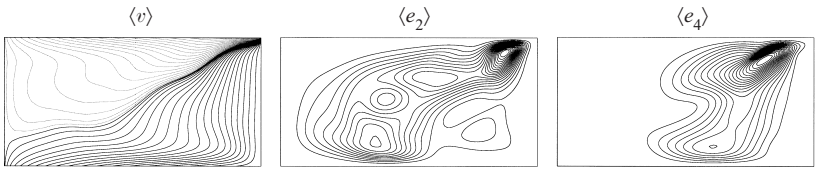


FIGURE 28. Contours of the azimuthally averaged azimuthal velocity and azimuthally averaged modal energy density for $MRW_{2,0}$ at $S = 0.800$; $\max(e_2) = 4.5 \times 10^{-3}$, $\max(e_4) = 1.1 \times 10^{-2}$.

these are given in figure 28. With $MRW_{2,0}$ the shear layer once again attaches to the axis, but closer to the bottom (compare $\langle v \rangle$ in figures 23 and 28). Also, the energy in the $m = 2$ mode is concentrated in the shear layer near where it separates from the top, in contrast to that in RW_2 which was concentrated near the axis and bottom Ekman layer. With the $m = 2$ energy being concentrated near the shear layer separation point, this results in a large-scale symmetry breaking of the shear layer from C_4 to C_2 (compare figures 24*a* and 24*c*), where in RW_2 the shear layer remains essentially C_4-symmetric and the symmetry breaking to C_2 is only evident near the axis.

For S greater than about 0.8 some solutions display the intermittent bursting phenomena also observed in the experiments. The modal-energy time series in figure 29 show competition between the $m = 2$, 4 and 5 azimuthal modes. The case in the figure was initiated from a RW_4 state, which is unstable at $S = 0.85$, to $m = 2$. The RW_4 evolves to an RW_2 state that is itself unstable to $m = 5$. When E_5 has grown to finite amplitude, there is continual exchange of energy among the three modes (and other modes via nonlinear convolution). The time series shows that the bursting phenomena consist of E_5 growing and drawing energy from E_4, while as E_4 is reduced the $m = 2$ component is not supported and E_2 diminishes, resulting in a lack of energy source for E_5 which also diminishes and then E_4 grows again. In this regime, the flow behaviour is very complex. These intermittent solutions co-exist with some of the previously described states, and both the experiments and the numerical simulations involving these are difficult to analyse. We leave this analysis to a separate and future investigation.

https://doi.org/10.1017/S0022112002008649 Published online by Cambridge University Press

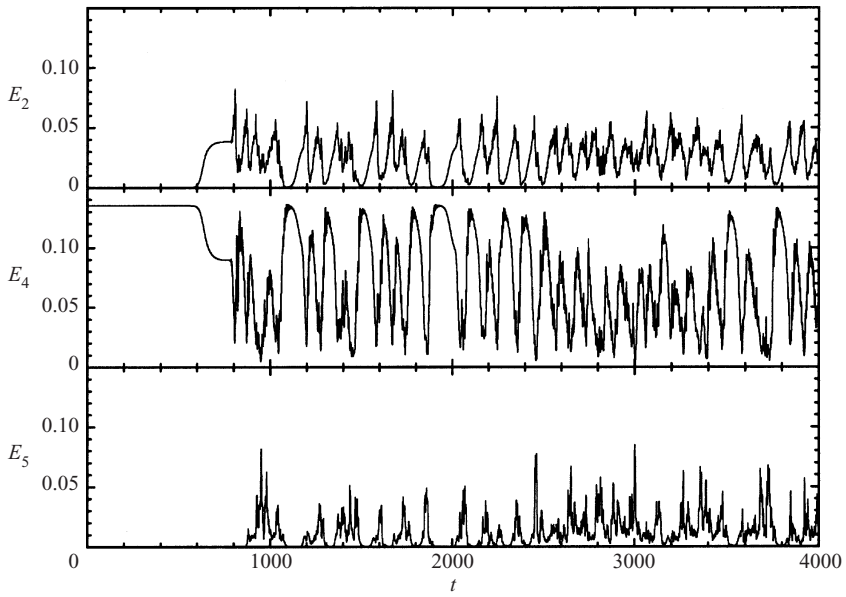


FIGURE 29. Time series of modal energies E_2, E_4 and E_5, for an intermittent state at $S = 0.85$, initiated from an RW_4 state.

5. Conclusion

Laboratory experiments and computational simulations have been carried out for a three-dimensional rotating flow driven by a differentially counter-rotating endwall. The two approaches are effectively equivalent. With fixed rotational Reynolds number $Re = 1000$, and aspect ratio $\Lambda = H/R = 0.5$, the main regimes as the differential rotation ratio S is varied are as follows.

(a) $S < 0.41$: Axisymmetric flow with a separated Ekman layer on the top.

(b) $0.41 < S < 0.79$: Multiple rotating waves of wavenumber 4 and 5, RW_4 and RW_5. The precession frequencies measured in the laboratory and extracted from the computations are essentially the same (compare figures 7 and 17).

(c) $S \approx 0.77$: A narrow window (of width about 0.01 in S) where RW_4 bifurcates to a subharmonic wavenumber-2 state, RW_2.

(d) $S \approx 0.79$: A narrow window (of width about 0.01 in S) with two stable states, RW_2 and a modulated (quasi-periodic) wave with wavenumber-2, $MRW_{2,0}$.

(e) $0.79 < S \lesssim 0.83$: Quasi-periodic flow.

(f) $0.83 < S$: Intermittent bursts of quasi-periodic motion.

The computations have enabled a detailed exploration of the bifurcations to different flow regimes. The first is a supercritical Hopf bifurcation from the steady axisymmetric basic state to RW_4. On increasing S, the unstable basic state undergoes a second Hopf bifurcation to an unstable RW_5, which becomes stable with a small increase in S, via a Neimark–Sacker bifurcation, spawning an unstable mixed mode. There is a small window in S where RW_4 loses stability via a Neimark–Sacker bifurcation and a stable mixed mode $MRW_{4,5}$ emerges. This state has not been observed experimentally; this is expected given the small range in S over which it exists and the small energy level contained in its $m = 5$ component.

The two stable rotating waves, RW_4 and RW_5, co-exist over the same range of S observed in the experiments. The spatial period doubling from RW_4, at the end of its

https://doi.org/10.1017/S0022112002008649 Published online by Cambridge University Press

range (point c above) to RW_2 is found to be a symmetry-breaking Neimark–Sacker bifurcation, and on increasing S is followed by a sequence of saddle-node bifurcations leading to the $MRW_{2,0}$ state, which has also been observed in the experiment (point d above).

For S at about 0.8 and above, quasi-periodic and intermittent states have also been computed that appear to correspond to states observed experimentally (points e and f above).

The computations and experiments illustrate the complex three-dimensional nature of the instabilities occurring in this system. The computed Eulerian fields in the wave regimes for $S > 0.41$ show how different instabilities are associated with different regions in the flow. Eddy energy can concentrate in the vicinity of the shear layer resulting from the separation of the Ekman layer on the counter-rotating top, or near the reconnection point on the axis, or near the bottom Ekman layer. The patterns are nonlinear with sharp corners (figure 14). Dye advection patterns from the experiment (figure 5) are also sharp cornered and complex. Both methods indicate that shear instability may lead to polygonal patterns such as those seen in geophysical situations mentioned in the Introduction. These patterns result from a linear instability of the shear layer to an azimuthal wavy mode. Where the downward velocity is locally large, a funnel-like structure forms and is drawn into the bottom Ekman layer, where it is counter-rotating. The advection of these vortical funnels by the jet-like meridional velocity at the shear layer produces a strong deformation of the linear mode, leading to the nonlinear polygonal structures.

Confined rotating flows have shear layers. In the simple problem where the bottom and sidewall are stationary, and the flow is driven by the rotating top, the dynamics of the resulting flow are governed by the behaviour of the shear layer that results when the Ekman layer on the rotating disk is turned by the presence of the sidewall. In that case, the shear layer remains close to the sidewall. In this study, we have effectively placed that simple system in a frame which is rotating counter to the top. This provides an extra degree of freedom (and an extra control parameter) which effectively allows the shear layer to come away from the sidewall. The rich dynamics reported here are due to the free shear layer exploring its new-found freedom.

This work was partially supported by NSF grants ATM-9714221, INT-9732637, CTS-9908599, DMS-0074283, OCE-0002345 (USA), and DGICYT grant PB97-0685 (Spain).

REFERENCES

Allison, M., Godfrey, D. A. & Beebe, R. F. 1990 A wave dynamical interpretation of Saturn's Polar Hexagon. *Science* **247**, 1061–1063.

Bergeron, K., Coutsias, E. A., Lynov, J. P. & Nielsen, A. H. 2000 Dynamical properties of forced shear layers in an annular geometry. *J. Fluid Mech.* **402**, 255–289.

Chomaz, J. M., Rabaud, M., Basdevant, C. & Couder, Y. 1988 Experimental and numerical investigation of a forced circular shear layer. *J. Fluid Mech.* **187**, 115–140.

Churilov, S. M. & Shukhman, I. G. 1992 Weakly nonlinear theory of the alternation of modes in a circular shear flow. *J. Fluid Mech.* **243**, 155–169.

Fantini, M. & Tung, K.-K. 1987 On radiating waves generated from barotropic shear instability of a western boundary current. *J. Phys. Oceanogr.* **17**, 1304–1308.

Ferreira, R. N. & Schubert, W. H. 1997 Barotropic aspects of ITCZ breakdown. *J. Atmos. Sci.* **54**, 261–285.

Früh, W.-G. & Read, P. L. 1999 Flow-field and point velocity measurements in a barotropically unstable shear layer. *Phys. Chem. Earth* B **24**, 461–466.

https://doi.org/10.1017/S0022112002008649 Published online by Cambridge University Press

Godfrey, D. A. 1988 A hexagonal feature around Saturn's north pole. *Icarus* **76**, 335–356.

Guckenheimer, J. & Holmes, P. 1986 *Nonlinear Oscillations, Dynamical Systems, and Bifurcations of Vector Fields*. Springer.

Hart, J. E. 1980 An experimental study of non-linear baroclinic instability and mode selection in a large basin. *Dyn. Atmos. Oceans* **4**, 115–137.

Hart, J. E. 1981 Wavenumber selection in nonlinear baroclinic instability. *J. Atmos. Sci.* **38**, 400–408.

Hide, R. & Titman, C. W. 1967 Detached shear layers in a rotating fluid. *J. Fluid Mech.* **29**, 39–60.

Hua, B. L. 1988 The internal barotropic instability of surface-intensified eddies. Part I: Generalized theory for isolated eddies. *J. Phys. Oceanogr.* **18**, 40–55.

Kuznetsov, Y. A. 1998 *Elements of Applied Bifurcation Theory, Second Edition*. Springer.

Limpasuvan, V., Leovy, C. B., Orsolini, Y. J. & Boville, B. A. 2000 A numerical simulation of the two-day wave near the stratopause. *J. Atmos. Sci.* **57**, 1702–1717.

Lopez, J. M. 1998 Characteristics of endwall and sidewall boundary layers in a rotating cylinder with a differentially rotating endwall. *J. Fluid Mech.* **359**, 49–79.

Lopez, J. M., Marques, F. & Shen, J. 2002 An efficient spectral-projection method for the Navier-Stokes equations in cylindrical geometries II. Three dimensional cases. *J. Comput. Phys.* **176**, 384–401.

Lopez, J. M. & Shen, J. 1998 An efficient spectral-projection method for the Navier-Stokes equations in cylindrical geometries I. Axisymmetric cases. *J. Comput. Phys.* **139**, 308–326.

Marques, F., Lopez, J. M. & Shen, J. 2002 Mode interactions in an enclosed swirling flow: a double Hopf bifurcation between azimuthal wavenumbers 0 and 2. *J. Fluid Mech.* **455**, 263–281.

Moroz, I. M. & Holmes, P. 1984 Double Hopf bifurcation and quasi-periodic flow in a model for baroclinic instability. *J. Atmos. Sci.* **41**, 3147–3160.

Orszag, S. A. & Patera, A. T. 1983 Secondary instability of wall-bounded shear flows. *J. Fluid Mech.* **128**, 347–385.

Paldor, N. 1999 Linear instability of barotropic submesoscale coherent vortices observed in the ocean. *J. Phys. Oceanogr.* **29**, 1442–1453.

Rabaud, M. & Couder, Y. 1983 A shear-flow instability in a circular geometry. *J. Fluid Mech.* **136**, 291–319.

Schubert, W. H., Montgomery, M. T., Taft, R. K., Guinn, T. A., Fulton, S. R., Kossin, J. P. & Edwards, J. P. 1999 Polygonal eyewalls, asymmetric eye contraction, and potential vorticity mixing in hurricanes. *J. Atmos. Sci.* **56**, 1197–1223.

Toyoda, E., Niino, H., Tsuboki, K., Kimura, R. & Yoshizaki, M. 1999 Midtropospheric anticyclonic vortex street associated with a cloud band near a cold front. *J. Atmos. Sci.* **56**, 2637–2656.

https://doi.org/10.1017/S0022112002008649 Published online by Cambridge University Press